

## BEAM PATTERN MEASUREMENTS FROM HERA OBSERVATIONS

C. D. NUNHOKEE<sup>1</sup> AND A. R. PARSONS<sup>1</sup>

<sup>1</sup>*Radio Astronomy Lab, University of California, Berkeley CA 94720, USA*

### ABSTRACT

In this work, we have evaluated the primary beam of HERA from observations of on-sky sources. We map the temporal flux density of sources in the FoV of the instrument as the sky drifts overhead. The observed flux density can be assumed to be constant over a timescale of 10.7 s, unlike satellite transmissions which rapidly varies due to changing distance and orientation. We have developed a tool that solves for the primary beam using measured and model value of the celestial sources. The software package can found on [https://github.com/Chuneeta/beam\\_solver](https://github.com/Chuneeta/beam_solver).

### 1. INTRODUCTION

Understanding the primary beam of the instrument is of paramount importance in particular for experiments dedicated to measuring the 21 cm HI. For most experiments a primary beam model is required throughout the data processing pipeline. For HERA, we use a simulated beam model for: 1) absolute calibration of the data in order to bring the visibilities to the proper scale, and 2) normalization of the 21 cm power spectra. Errors in the assumed beam model can lead to absolute amplitude errors in our visibilities and improper normalization of the power spectra, therefore it is crucial to validate the primary beam model that is being used. This work tries to confirm if the beam model used in the processing of HERA data is consistent with the actual beam of the instrument.

### 2. OBSERVATION AND CALIBRATION

We used data from the HERA-52 antenna configuration (Figure 1), operating within the 100–200 MHz frequency band in a drift-scan mode. The data was recorded 12 hours per day for 18 days, and the observations were scheduled during the night time between 6 pm to 6 am SAST. The antenna records data point every 10.7 seconds for each of 1024 evenly-spaced frequency channels.

The first stage in the data processing is identification of non-working antennas and RFI channels. Only the channels between 120 and 180 MHz were used as the bandpass filter response rolls off fairly sharp beyond those edges. Dysfunction antennas (red crosses, Figure 1) and channels that were known to be affected by Orbcomm satellite transmission (136–138 MHz) were flagged. In addition, a median filter was applied to the visibility along both the frequency and time axes.

After RFI flagging, we employed redundant calibration, a powerful technique which uses the property that baselines of the same length and orientation observe the same sky signal. Redundant calibration iteratively solves for the relative antenna solutions without prior knowledge of the sky signal by minimizing the sum of the deviations of the measured visibilities to that of the model

$$\chi^2 = \sum_{bl} \frac{|V_{ij} - g_i g_j^* V'_{ij}(t, \nu)|^2}{\sigma_{ij}^2} \quad (1)$$

where  $\sigma_{ij}^2$  is the noise on the measured visibility. The model visibilities  $V'_{ij}(t, \nu)$  is initially taken to be the averaged visibilities over all the redundant baselines and is updated at each iteration. However, the estimated gain solutions are degenerate, and these degeneracies include the overall amplitude, overall phase and the phase gradients. We then used the traditional sky-based calibration to solve for the overall phase and amplitude (HERA memo #58).

### 3. IMAGING

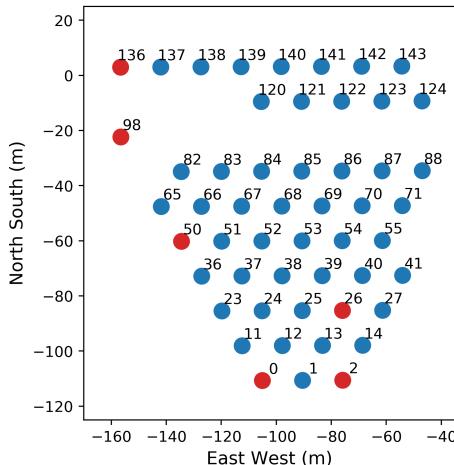


**Figure 1.** HERA-52 antenna configuration. The elements highlighted in red were dysfunctional for the observing season.

The calibrated visibilities are then Fourier transformed into individual images integrated over 10 minutes. Uniform weighting were applied to the gridded visibilities in order to minimize contaminations from sidelobes. The multi-frequency synthesis algorithm was used on channels between 120 and 180 MHz generating images at 151 MHz. Each image was deconvolved using the Cotton-Schwab algorithm until the desired threshold was reached or number of iterations are completed. Figure 2 shows the resulting images generated from three consecutive datasets for linear ( $x$ ) and vertical ( $y$ ) polarizations. We see how the intensity of the sources varies as they transit through the instrument. Hence we attempt to map the source tracks of all potential sources transiting through the primary beam of HERA.

We ran PyBDSF on images generated using observations from a single day, and found 120 potential source candidates. Out of these 120 sources, the power/flux tracks of three sources are shown in Figure 3. These three sources can also be seen in Figure 2.

#### 4. ELECTROMAGNETIC SIMULATION

The HERA antenna setup consists of a 14 m diameter faceted parabolic reflector and a PAPER dipole (left panel, Figure 4). The dipole measures the linear/horizontal and vertical polarizations of the signal and it is sandwiched between two steel discs that act as sleeves to broaden the frequency response by creating a dual-resonance structure. The response of the HERA antenna is simulated using the Computer Simulation Technology (CST) software (HERA Memo #29). The electromagnetic simulation is performed by modeling the antenna and feed (right panel, Figure 4), and taking into account the various effects of the materials being used. The resulting antenna response for different polarizations are shown in Figure 5. The antenna response in the horizontal direction is a  $90^\circ$  rotation of that in the vertical.

#### 5. FORMALISM

For any given source  $s$  with a flux density  $I'_s(\nu)$  at frequency  $\nu$ , the measured flux density  $I_s$  at any horizontal coordinate  $(\theta, \phi)$  can be given by

$$I_s(\theta, \phi, \nu) = A_s(\theta, \phi, \nu) I'_s(\nu) \quad (2)$$

where  $A_s(\theta, \phi, \nu)$  is the primary beam response of the source  $s$  in the direction  $(\theta, \phi)$ . Suppose we have  $n$  measured values of  $I_s$  (data) and want to use the data to estimate a set of  $m$  numbers  $(a_1, a_2, \dots, a_m)$  representing a flattened 2-dimensional map of  $A(\nu)$ . The map in principle needs to be pixelized, therefore  $a_k$  represent the primary beam value at pixel  $k$ . Thus, we can express  $A_s(\theta, \phi, \nu)$  as the sum of the four closest pixels to  $(\theta, \phi)$  such that

$$A_s(\theta, \phi, \nu) = \sum_{l=1}^4 a_{k_l} w_{k_l}; \quad \sum_{l=1}^4 w_{k_l} = 1 \quad (3)$$

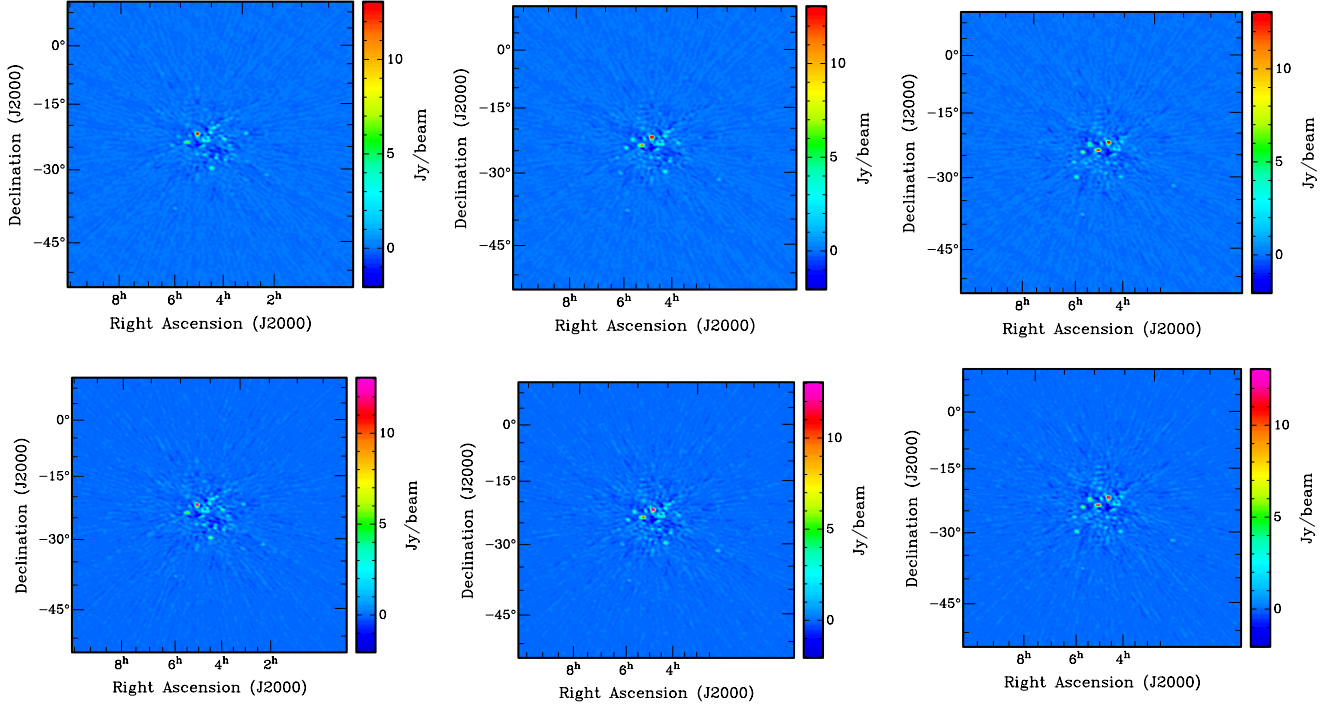


**Figure 2.** Multi-frequency synthesized images for three consecutive datasets for x (top) and y (bottom) polarizations.

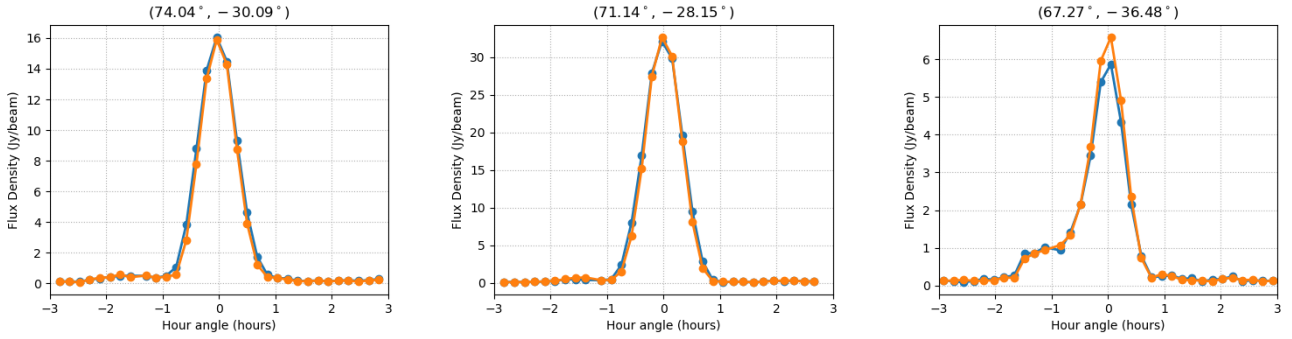


**Figure 3.** Peak flux values of three sources as a function of time for x (blue) and y (orange) polarizations.

where  $(k_1, k_2, k_3, k_4)$  denotes the four chosen pixels and  $w_k$  the weights assigned to them. Using Equation 3,

$$I_s(\theta, \phi, \nu) = \sum_{l=1}^4 a_{k_l} w_{k_l} I'_s(\nu). \quad (4)$$

Given that we have  $n$  sources and for each source, we measure the flux density at different time intervals during its transit, we can form a system of linear equations in the form

$$\mathbf{y} = \mathbf{A}\mathbf{x} \quad (5)$$

where  $\mathbf{A}$  contains the coefficients of equation 4 and  $\mathbf{y}$  is the flux measurements. The optimal estimate of  $A(\nu)$  is

$$\tilde{\mathbf{x}} = (\mathbf{A}^T \mathbf{N}^{-1} \mathbf{A})^{-1} \mathbf{A}^T \mathbf{y} \quad (6)$$

where  $\mathbf{N}$  is the noise covariance between the flux measurements. Since the noise between the flux measurements are uncorrelated with each other,  $\mathbf{N}$  transforms into a diagonal matrix. Assuming that the variances between the flux measurements are identical,

$$\tilde{\mathbf{x}} = (\mathbf{A}^T \mathbf{A})^{-1} \mathbf{A}^T \mathbf{y} \quad (7)$$

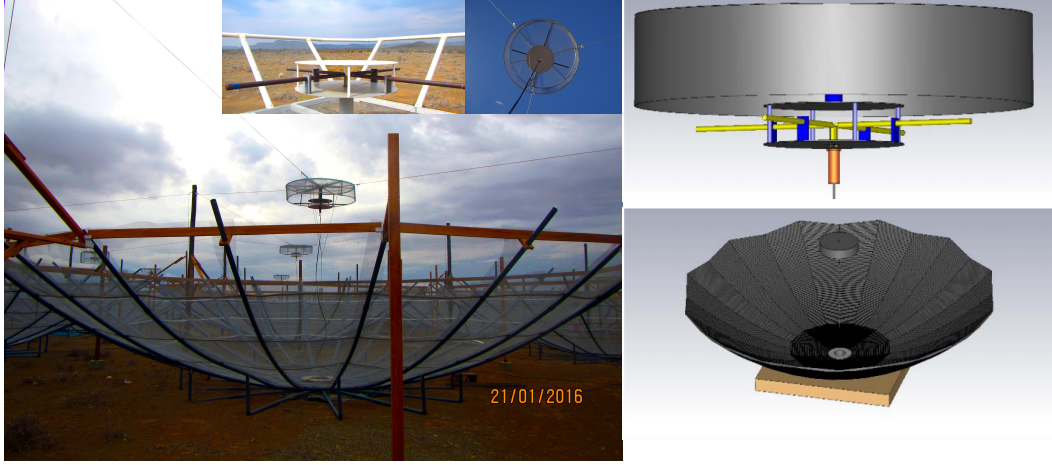


**Figure 4.** HERA dish and feed as modeled by CST.

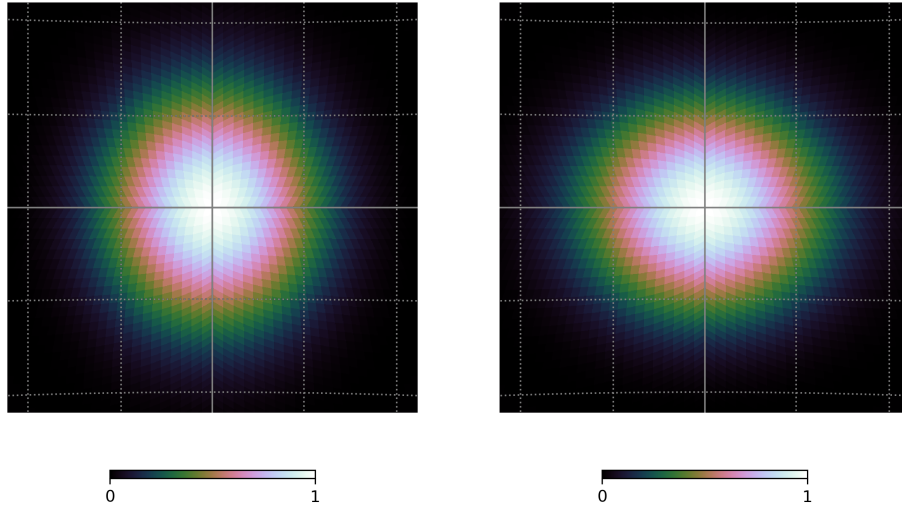


**Figure 5.** Horizontal (left) and vertical (top) polarization responses of the HERA antenna at 151 MHz simulated using CST.

## 6. CONSTRUCTING BEAM PATTERN

### 6.1. Using single polarization

We calculated  $I'_s(\nu)$  using our measurements:

$$I'_s(\nu) = \frac{\sum_{(\theta, \phi)} A(\theta, \phi, \nu) I_s(\theta, \phi, \nu)}{\sum_{(\theta, \phi)} A(\theta, \phi, \nu)^2} \quad (8)$$

The computed values of  $I'_s(\nu)$  at 151 MHz for both polarizations are illustrated in Figure 6. We then fed in the measured and computed values for x polarization to equation 3 and solves for the beam pixel values. We used a grid of  $121 \times 121$ . The left panel of Figure 7 shows the generated beam. We can see some degenerate mode which are due to the limited number of equations comprising of these beam pixels. In order to get rid of these degenerate modes, we decomposed  $\mathbf{A}$  using single value decomposition and discarded all bad eigen-modes (shown in Figure 8). The right panel of Figure 7 shows the constructed beam after removing the degenerate modes. However, the resolution of the

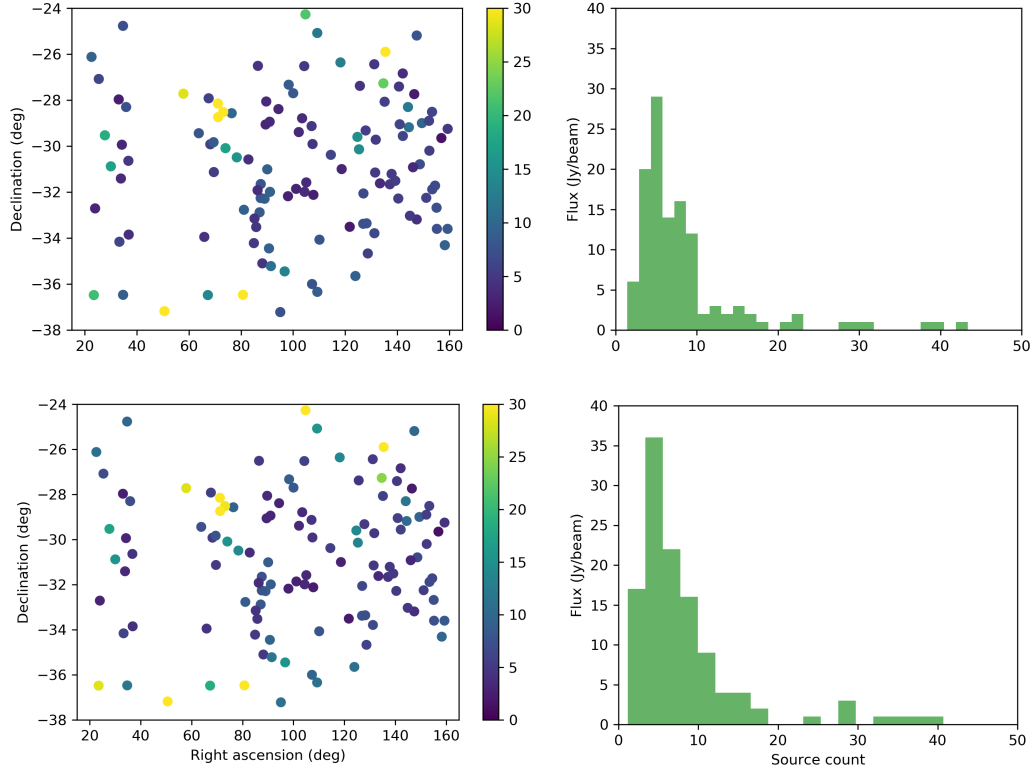


**Figure 6.** Potential source candidates obtained from images for x (top) and y (bottom) polarizations. The color intensity represents the peak flux value of the sources. The right panel shows a histogram plot of the flux distribution for both polarizations.

resulting is coarse, therefore we interpolated the data points along the hour angle axis and fed the interpolated values into equation 3 again. Figure 9 shows the beam obtained using data along the x and y polarizations separately. A slice of the beam through zenith in the East-West and North-South direction can be seen in Figure 10.

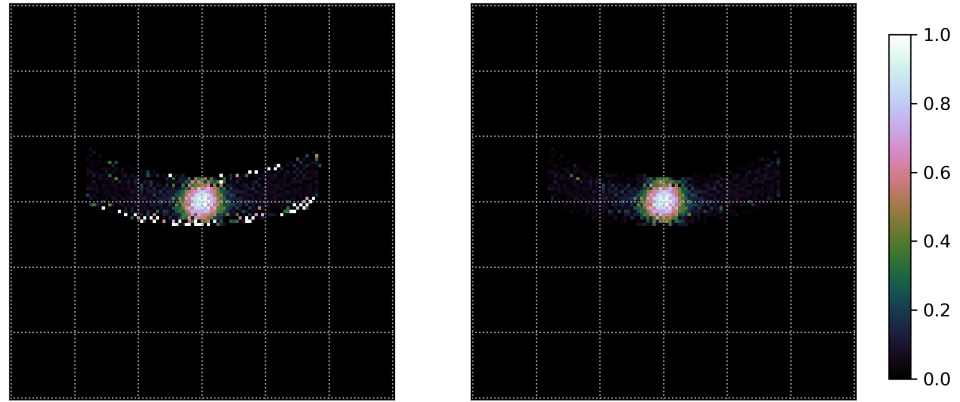


**Figure 7.** Beam pattern constructed using the formalism in Section 5. The right panel shows the constructed beam pattern after removing the degenerate modes.

## 6.2. Using cross polarization

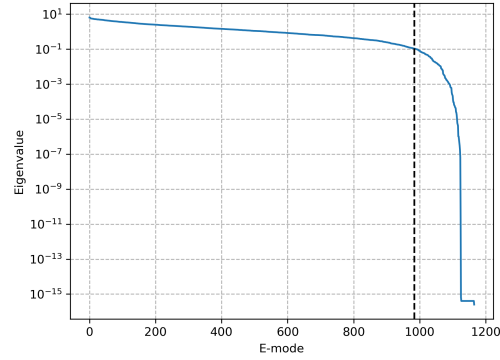


**Figure 8.** Eigenvalue obtained by decomposing  $\mathbf{A}$ . The black line shows the line after which the eigen modes were discarded.

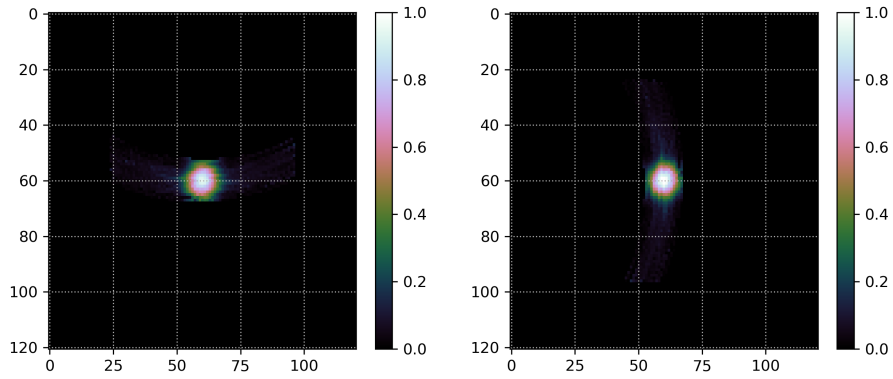


**Figure 9.** Beam pattern constructed using interpolated data points for x (left) and y (right) polarizations.

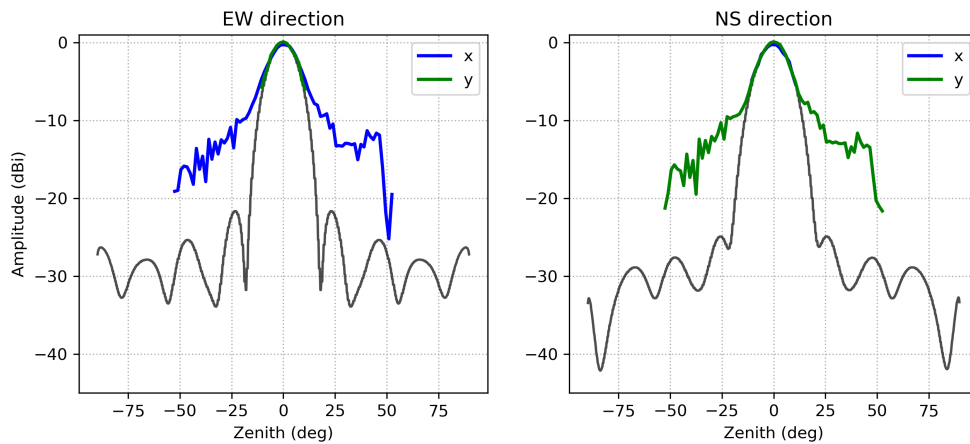


**Figure 10.** Slice of the beam pattern for x (blue) and y (green) polarizations obtained in Figure 9 passing through zenith in the east-west (left) and north-south (right) direction. The black line denotes the simulated beam model.

The caveat in the above case is that we are inheriting the beam model in North South direction given that source transits from East to West. Therefore to eliminate this caveat, we utilize the property that the beam in the x direction

is a 90 degree rotation of the beam in the y direction. Hence we can use equation 4 such that:

$$I_{xx}(\theta, \phi, \nu) = \sum_{l=1}^4 a_{k_l} w_{k_l} I'_{xx}(\nu) \quad (9)$$

$$I_{yy}(\theta, \phi, \nu) = \sum_{l=1}^4 a'_{k_l} w'_{k_l} I'_{yy}(\nu) \quad (10)$$

where  $I_{xx}$  and  $I_{yy}$  are the flux density of a source for x and y polarizations respectively,  $a'_k$  is the pixel value representing the 90° rotated beam and  $w'_k$  is the corresponding weight assigned to that pixel. Figure 11 shows the 2-dimensional beam pattern generated using data from both polarizations and Figure 12 illustrates a slice of the resulting beam through zenith in the East-West and North-South directions.

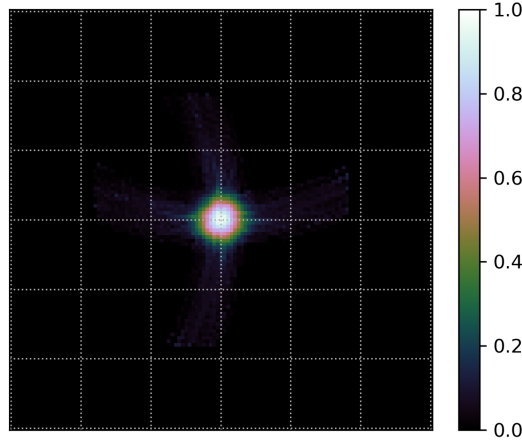


**Figure 11.** Beam pattern constructed using interpolated data points from both x and y polarizations.

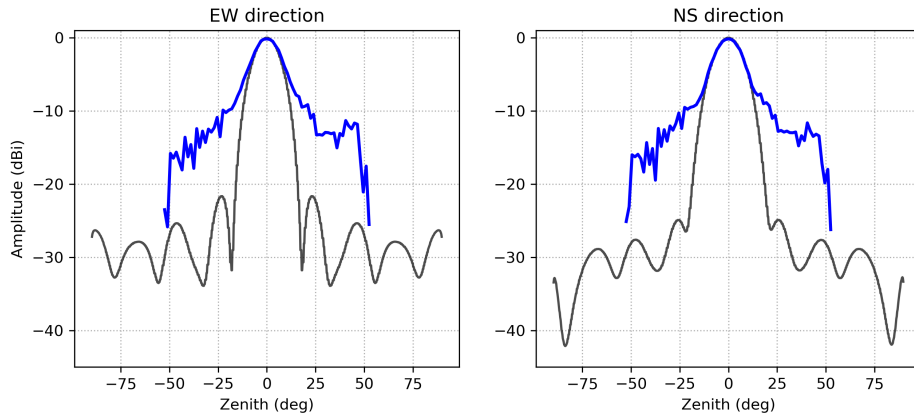


**Figure 12.** Slice of the beam pattern obtained in Figure 11 passing through zenith in the east-west (left) and north-south (right) direction. The black line denotes the simulated beam model.

## 7. COMPARISON OF BEAM PATTERNS

Table 7 list the peak amplitude (peak at zenith) of the constructed beam using only x and y polarizations and both of them. Figure 13 shows the comparison over a  $15^\circ$  FoV.

Value at zenith	East-West	North-South
Simulated beam model	1.0	1.0
Constructed beam from x	0.94	0.96
Constructed beam from y	1.02	1.02
Constructed beam from x and y	0.96	0.96

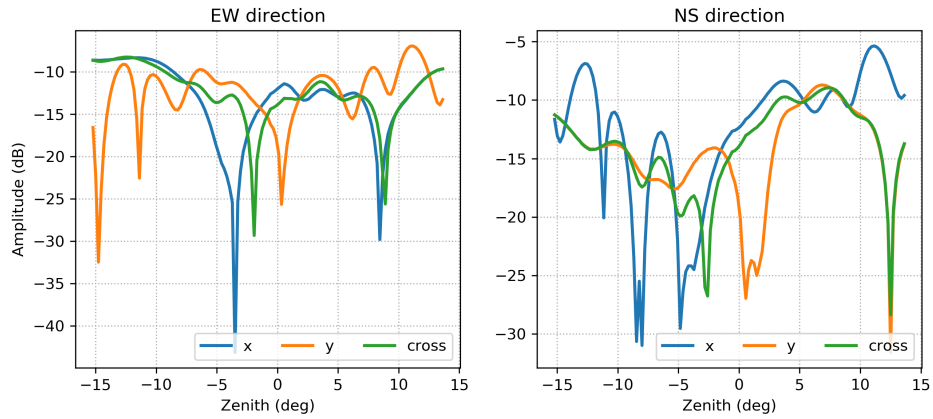


**Figure 13.** Difference in amplitude from resulting beam patterns (x, y and cross polarizations) in the East-West (left) and North-South (right) direction.